

## The global relaxation redistribution method for reduction of combustion kinetics

Mahdi Kooshkbaghi, Christos E. Frouzakis, Eliodoro Chiavazzo, Konstantinos Boulouchos, and Iliya V. Karlin

Citation: *The Journal of Chemical Physics* **141**, 044102 (2014); doi: 10.1063/1.4890368

View online: <http://dx.doi.org/10.1063/1.4890368>

View Table of Contents: <http://scitation.aip.org/content/aip/journal/jcp/141/4?ver=pdfcov>

Published by the [AIP Publishing](#)

---

### Articles you may be interested in

[Determination of char combustion kinetics parameters: Comparison of point detector and imaging-based particle-sizing pyrometry](#)

*Rev. Sci. Instrum.* **85**, 075114 (2014); 10.1063/1.4890438

[Lasing action induced by femtosecond laser filamentation in ethanol flame for combustion diagnosis](#)

*Appl. Phys. Lett.* **104**, 091106 (2014); 10.1063/1.4867503

[Route to chaos for combustion instability in ducted laminar premixed flames](#)

*Chaos* **22**, 023129 (2012); 10.1063/1.4718725

[A regime diagram for premixed flame kernel-vortex interactions](#)

*Phys. Fluids* **19**, 043604 (2007); 10.1063/1.2720595

[Combustion mechanism of liquid fuel spray in a gaseous flame](#)

*Phys. Fluids* **17**, 123301 (2005); 10.1063/1.2140294

---



**AIP** | Journal of  
Applied Physics

*Journal of Applied Physics* is pleased to  
announce **André Anders** as its new Editor-in-Chief

# The global relaxation redistribution method for reduction of combustion kinetics

Mahdi Kooshkbaghi,<sup>1</sup> Christos E. Frouzakis,<sup>1,a)</sup> Eliodoro Chiavazzo,<sup>2</sup>  
 Konstantinos Boulouchos,<sup>1</sup> and Iliya V. Karlin<sup>1</sup>

<sup>1</sup>*Aerothermochemistry and Combustion Systems Laboratory, Swiss Federal Institute of Technology, Zurich CH-8092, Switzerland*

<sup>2</sup>*Politecnico di Torino, Energy Department, Corso Duca degli Abruzzi 24, 10129 Torino, Italy*

(Received 25 April 2014; accepted 3 July 2014; published online 22 July 2014)

An algorithm based on the Relaxation Redistribution Method (RRM) is proposed for constructing the Slow Invariant Manifold (SIM) of a chosen dimension to cover a large fraction of the admissible composition space that includes the equilibrium and initial states. The manifold boundaries are determined with the help of the Rate Controlled Constrained Equilibrium method, which also provides the initial guess for the SIM. The latter is iteratively refined until convergence and the converged manifold is tabulated. A criterion based on the departure from invariance is proposed to find the region over which the reduced description is valid. The global realization of the RRM algorithm is applied to constant pressure auto-ignition and adiabatic premixed laminar flames of hydrogen-air mixtures. © 2014 AIP Publishing LLC. [<http://dx.doi.org/10.1063/1.4890368>]

## I. INTRODUCTION

The detailed reaction mechanisms of practical fuels contain hundreds of species participating in hundreds to thousands of chemical reactions. In addition to the large number of variables that need to be accounted for, disparate time scales introduce stiffness and increase the computational cost of numerical simulations. On the other hand, time scales associated with transport phenomena cover a narrower range of typically slower time scales. When the coupling of flow phenomena with chemical kinetics is of interest, changes due to the fastest time scales can be assumed to be equilibrated, and, after a short transient, the system dynamics evolve on a manifold of lower dimension. Dimension reduction can then be employed to decrease the computational cost by representing the chemical system with a smaller number of variables describing the slow dynamics.

Dimension reduction techniques search for a systematic way to decouple the fast and slow dynamics. More specifically, these methods aim at approximating the Slow Invariant Manifold (SIM), i.e., the lower dimensional sub-manifold in the phase space to which all solution trajectories are attracted after a short transient. Detailed classification and reviews of model reduction approaches for chemical kinetics and dynamical systems in general can be found in Refs. 1–4.

For the purposes of this work, low-dimensional manifold construction techniques can be broadly classified into two categories.<sup>5</sup> The first category is based on time scale analysis to identify the slow and fast modes of the system. The Computational Singular Perturbation (CSP) method proposed an iterative refinement procedure aiming at approximating the basis vectors spanning the slow and fast subspaces.<sup>6</sup> Based on the spectral decomposition of the Jacobian, which recovers

the CSP basis at leading order, the Intrinsic Low Dimensional Manifold (ILDM) method<sup>7</sup> constructs a first-order approximation of the slow manifold.<sup>8</sup>

The second category includes geometrical approaches for the SIM construction. For example, the thermodynamic properties which are known functions of the system state can be used to determine the low dimensional thermodynamic manifolds, which are “good” in the sense that they are not folded, multi-valued, discontinuous, non-realizable, or non-smooth.<sup>4</sup> The Rate-Controlled Constrained Equilibrium (RCCE) method assumes that the variables evolve from the initial to the equilibrium (steady) state through a sequence of quasi-equilibrium states, which can be computed by minimizing a thermodynamic Lyapunov function under appropriate predefined constraints.<sup>9,10</sup> The temporal evolution of the system can be expressed as a function of the rate of change of the constraints. Similarly, an Invariant Constrained Equilibrium (ICE) manifold is constructed from trajectories emanating from the constrained equilibrium edge, which can be defined by a RCCE-like approach; the local species reconstruction can be obtained with the help of preimage curves.<sup>11</sup> Trajectories which are closest to equilibrium are alternative candidates for the slow manifold. In the Minimal Entropy Production Trajectories (MEPT) approach, entropy production is used as an indicator to discriminate the trajectories.<sup>12</sup> The manifolds obtained using thermodynamic functions, which often are neither slow nor invariant,<sup>5</sup> are only approximations of the SIM.

Other constructive methods are based on the iterative solution of the partial differential equations defining the slow manifold (e.g., Ref. 13), on finding the invariant manifold connecting the equilibrium state to (usually unphysical) saddle points,<sup>5,14</sup> and on trajectory-optimization variational approaches,<sup>12,15</sup> which was recently applied for the construction of a two-dimensional SIM for syngas combustion.<sup>16</sup>

<sup>a)</sup>Electronic mail: frouzakis@lav.mavt.ethz.ch

Formally, the slow dynamics can be described by the film equation (see Sec. II), which in the general case can be solved iteratively starting from an initial guess that is gradually relaxed to the slow manifold. The Method of Invariant Grids (MIG) for chemical kinetics defines the slow manifold as a collection of discrete points in concentration space, which lie on the steady solution of the film equation.<sup>17</sup>

In the spirit of the MIG, the Relaxation Redistribution Method (RRM) was proposed as a way to construct slow manifolds of any dimension by refining an initial guess (initial grid) until it converges to a neighborhood of the SIM.<sup>18</sup> In its local realization, stability of the RRM refinements provides a criterion for finding the dimension of the local reduced model.<sup>18</sup> This dimension may become large when extending the manifold to cover the whole composition space (up to the full system dimension in the hydrogen combustion example considered in Ref. 18). As such, the local formulation of RRM requires smart storage/retrieval tabulation methods for computational efficiency.

In this paper, we propose a RRM-based method for the construction and tabulation of manifolds of fixed pre-selected dimension. For this purpose, RCCE is employed to obtain an initial guess for the manifold and the manifold boundary, which is kept fixed, while the RRM algorithm is applied to the interior points. For the region within the RCCE-defined boundary where the slow dynamics can be described by a SIM with the chosen dimension, the algorithm converges to the slow invariant manifold. An indicator for the quality of the reduction is proposed based on a measure of the manifold invariance. For the region where a higher-dimensional reduced description is required, the algorithm still converges to a manifold which approximates the invariant manifold better than the RCCE manifold of the same dimension. The algorithm is applied to hydrogen-air mixtures and the tabulated reduced description is validated in homogeneous systems as well as in a laminar premixed flame.

The paper is organized as follows. In Sec. II, the basic notion of the slow invariant manifold and the film equation of dynamics are briefly discussed, and the features of the RRM method are presented using a singularly-perturbed nonlinear system of ordinary differential equations. In Sec. III, detailed reaction kinetics is reviewed briefly. The initialization of the slow manifold, the refinement procedure based on RRM, and the use of pre-tabulated manifold are presented in Sec. IV. Finally, the results of RRM manifold for auto-ignition and laminar premixed flame of hydrogen-air mixture are presented in Sec. V.

## II. SLOW INVARIANT MANIFOLD AND RRM

Consider an autonomous system satisfying the Cauchy-Lipschitz existence and uniqueness theorem with a single stable fixed point (unique equilibrium) whose detailed (*microscopic*) dynamics are described by the evolution of its state vector  $\mathbf{N}(t)$  in a  $n_s$ -dimensional phase space  $S$ ,  $\mathbf{N}(t) \in S \subset \mathbb{R}^{n_s}$ ,

$$\frac{d\mathbf{N}}{dt} = \mathbf{f}(\mathbf{N}), \quad (1)$$

where  $\mathbf{f}$  is a vector valued function,  $\mathbf{f} : S \rightarrow \mathbb{R}^{n_s}$ .

A domain  $U \subset S$  is a positively invariant manifold if every trajectory of system (1) starting on  $U$  at time  $t_0$  remains on  $U$  for any  $t > t_0$ . Therefore,  $\mathbf{N}(t_0) \in U$  implies  $\mathbf{N}(t) \in U$  for all later times  $t > t_0$ .

The dynamics of (1) is typically characterized by different time scales. For significant time scale disparity, after an initial transient solution, trajectories are quickly attracted to a lower dimensional manifold where they continue to evolve at a slower time scale towards the steady state  $\mathbf{N}^{eq} \in S$ . This positively invariant manifold is the SIM,<sup>1</sup> and its construction can be based on the definition of fast and slow sub-spaces within the phase space.<sup>19-21</sup>

Neglecting the initial fast transient, the long-time dynamics can be described by a (possibly significantly) smaller number of the slowly-evolving *macroscopic* variables  $\xi$ , which can be used to parametrize the SIM. The  $n_d < n_s$  macroscopic variables  $\xi$  belong to an  $n_d$ -dimensional space  $\Xi$ , and can be used for the description of the reduced dynamics of (1). The manifold parametrization space  $\Xi$  can be spanned by different combinations of the state variables,  $\mathbf{N} \in S$ . A microscopic state  $\mathbf{N}$  located on the low-dimensional manifold is shown schematically in Fig. 1(a). More formally, any point  $x$  on  $\mathbf{W}$  satisfies  $x = \mathcal{F}(\xi)$  where  $\mathcal{F} : \Xi \rightarrow S$  maps points  $\xi \in \Xi$  on the manifold parametrization space onto the corresponding point on the manifold  $\mathbf{W}$  which is embedded in the phase space  $S$  (see Ref. 1).

The evolution of a state  $\mathbf{N}$  can be decomposed into the slow component along  $T_{\mathbf{W}}$ , the tangent space of  $\mathbf{W}$ , and its complement in the transverse direction (Fig. 1(a)),

$$\mathbf{f}(\mathbf{N}(\xi)) = \mathbf{f}(\mathbf{N}(\xi))_{\parallel T_{\mathbf{W}}} + \mathbf{f}(\mathbf{N}(\xi))_{\perp T_{\mathbf{W}}}. \quad (2)$$

The slow and fast components are defined, respectively, as

$$\mathbf{f}(\mathbf{N}(\xi))_{\parallel T_{\mathbf{W}}} = \mathbf{P}\mathbf{f}(\mathbf{N}(\xi)), \quad (3)$$

$$\mathbf{f}(\mathbf{N}(\xi))_{\perp T_{\mathbf{W}}} = \Delta(\mathbf{N}(\xi)) = \mathbf{f}(\mathbf{N}(\xi)) - \mathbf{P}\mathbf{f}(\mathbf{N}(\xi)), \quad (4)$$

in terms of an  $n_s \times n_s$  projection matrix  $\mathbf{P}$  and the defect of invariance  $\Delta(\mathbf{N}(\xi))$ .

By definition,  $\mathbf{W}$  is a positively invariant manifold if any state that is initially on  $\mathbf{W}$  remains on it during the subsequent time evolution. Hence, relaxation will only proceed along the tangent space and the normal component should be zero,

$$\Delta(\mathbf{N}(\xi)) = 0, \quad \xi \in \Xi. \quad (5)$$

Equation (5) is known as the invariance condition, which can be solved for the unknown slow invariant manifold. In the Method of Invariant Manifold (MIM), the SIM is the stable solution of the so-called film extension of dynamics,<sup>1</sup>

$$\frac{d\mathbf{N}(\xi)}{dt} = \Delta(\mathbf{N}(\xi)), \quad (6)$$

which defines an evolutionary process guiding an initial guess for the manifold towards the slow invariant manifold. In numerical realizations, manifolds are usually represented by a grid (discrete set of points), as proposed in the MIG.<sup>17</sup> Due to the locality of MIM construction, we make no further distinction between manifold and grid.

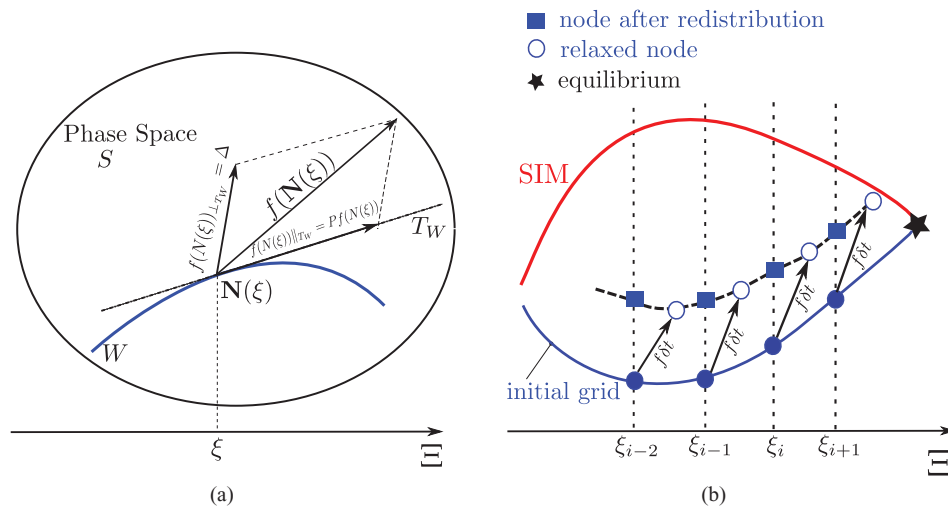


FIG. 1. (a) Schematic of the motion decomposition which is exploited in the construction of the slow manifold; (b) Relaxation Redistribution algorithm: the effect of slow motions are neutralized via redistribution.

If the initial grid is subjected to the system dynamics, the distance between the grid nodes shrinks and the whole grid contracts to a neighborhood around the equilibrium state. The key idea of RRM is to alternate a relaxation step with an appropriate movement that counterbalances shrinking. One iteration step of RRM is shown schematically in Fig. 1(b). After relaxation, the nodes of the initial grid (filled circles) evolve to different positions (open circles) and the macroscopic coordinates change. The increased density of the grid points close to equilibrium can result in a reduction of the grid spacing. To prevent this, the redistribution step brings the macroscopic coordinates  $\xi$  back to their previous values by interpolation between the inner relaxed states and extrapolation for grid points outside the contracted boundaries. The converged solution is the manifold containing all the states for which further relaxations result in movement only along the manifold.

In order to clarify the aforementioned notions, the singularly-perturbed dynamical system proposed in Ref. 22 is considered with  $\mathbf{N} = (x, y)^T$ ,

$$\frac{dx}{dt} = 2 - x - y, \quad (7a)$$

$$\frac{dy}{dt} = \gamma(\sqrt{x} - y). \quad (7b)$$

For  $x(t), y(t) \in \mathbb{R}$ ,  $x(t) \geq 0$ , and  $\gamma \gg 1$ , the system evolves from any initial condition  $(x_0, y_0)$  towards the fixed point at  $(1, 1)$ .

For  $\gamma = 20$ , choosing  $\xi = x$  to parametrize the manifold and  $y = 1 - x$  as the initial grid, after a single integration step (relaxation) with  $\delta t = 0.07$ , the initial grid (open squares) contracts significantly (Fig. 2(a), open circles). Redistribution is then applied to find the  $y$  values at the original locations of the parametrizing macroscopic coordinates by linear interpolation between relaxed states on the interior grid and linear extrapolation at the boundary (two leftmost star symbols). The RRM converges to the slow invariant manifold after 10 iterations for a tolerance of  $10^{-4}$  (Fig. 2(b), solid line).

The defect of invariance  $\Delta$  can be used as an indicator for the time after which the reduced description becomes accurate. For the chosen parametrization, the kernel of the projector  $\mathbf{P}$  is  $(1, 0)$ .  $\mathbf{P}$  is spanned by its image, which is the tangent subspace to the manifold,  $T_W = \text{im}\mathbf{P}$ , and the orthogonal to the kernel. Hence,

$$\mathbf{P} = \begin{pmatrix} 1 \\ \frac{dy}{dx} \end{pmatrix} (1, 0) = \begin{pmatrix} 1 & 0 \\ \frac{dy}{dx} & 0 \end{pmatrix}. \quad (8)$$

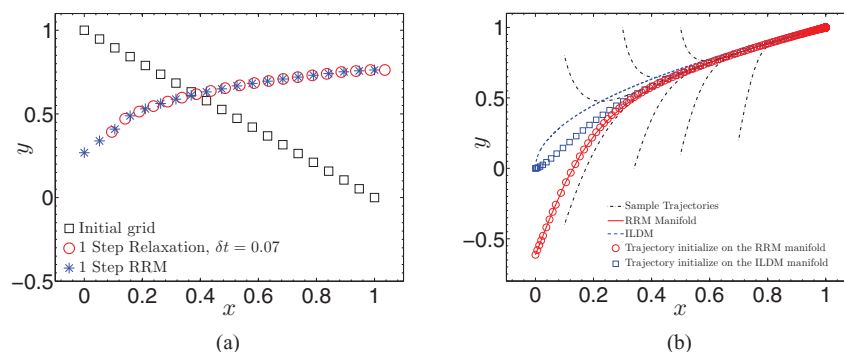


FIG. 2. (a) The effect of applying a single RRM step on the nodes of the initial grid; (b) comparison between ILDM manifold, RRM manifold, and sample trajectories  $\gamma = 20$ .

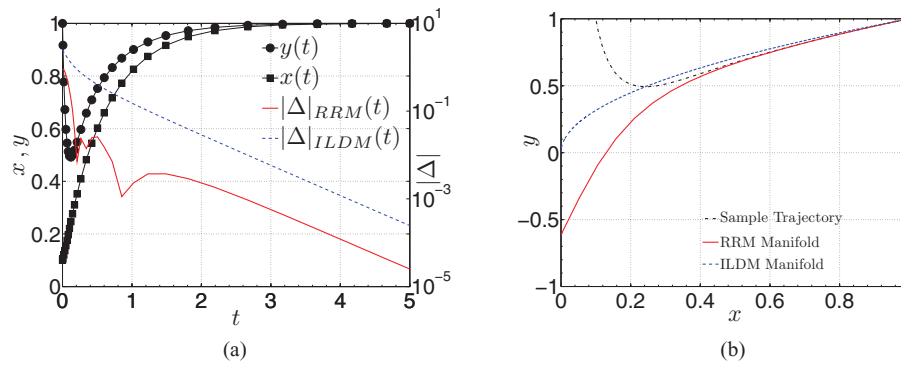


FIG. 3. Analysis of ILDM and RRM manifold for (7). (a) Defects of invariance and temporal evolution of the state for a sample trajectory. (b) Sample trajectory, ILDM and RRM manifolds in phase space for  $\gamma = 20$ .

From (4), the defect of invariance is then

$$\Delta = (\mathbf{I} - \mathbf{P})\mathbf{f} = \begin{pmatrix} 0 \\ \frac{dy(\xi)}{-d\xi} (2 - \xi - y(\xi)) + \gamma (\sqrt{\xi} - y(\xi)) \end{pmatrix}. \quad (9)$$

In this case, the manifold is smooth and  $\frac{dy(\xi)}{d\xi}$  along the manifold can be accurately approximated numerically by second order central differences.

In order to compare the manifold and its invariance with the ILDM, the Jacobian  $\mathbf{J}$  of (7),

$$\mathbf{J} = \begin{pmatrix} -1 & -1 \\ \frac{\gamma}{2\sqrt{x}} & -\gamma \end{pmatrix} \quad (10)$$

is needed. The symmetrized Jacobian  $\mathbf{J}_{sym} = \mathbf{J}\mathbf{J}^T$ , which offers the advantage of real eigenvalues,  $\lambda$ , and orthogonal eigenvectors,  $\mathbf{v}$ , can be used to define the fast and slow invariant subspaces of (7).<sup>23,24</sup> Let us define the matrix  $\mathbf{V}$  with a column partitioning given by the eigenvectors of  $\mathbf{J}_{sym}$  ordered according to decreasing values of the corresponding eigenvalues,  $\mathbf{V} = (\mathbf{v}_{slow}, \mathbf{v}_{fast})$  and its inverse  $\mathbf{V}^{-1} = (\tilde{\mathbf{v}}_{slow}, \tilde{\mathbf{v}}_{fast})^T$ . For  $\gamma \gg 1$ , the ILDM manifold,  $y_{ILDM}$ , obtained by setting the inner product of  $\tilde{\mathbf{v}}_{fast}$  with  $\mathbf{f}$ <sup>7,24</sup> equal to zero has the approximate form

$$y = \sqrt{x}. \quad (11)$$

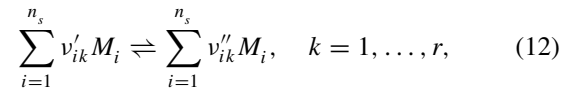
The ILDM manifold is plotted in Fig. 2(b) (dashed line) together with several trajectories (dotted-dashed lines) and the RRM manifold (solid line). Trajectories initialized at the left-most boundary of the ILDM (open squares) and RRM (open circles) manifolds are also shown. In this case, the ILDM manifold is neither invariant nor slow, except close to the steady state. On the other hand, different solution trajectories are quickly attracted (Fig. 3(a)) to the RRM manifold, which is also seen to be invariant.

For the initial condition  $(x_0, y_0) = (0.1, 1.0)$ , the temporal evolution of the state and the Euclidean norm of  $\Delta$  for the RRM and ILDM manifolds of system (7) are plotted in Fig. 3(a). The defect of invariance for the RRM manifold is an order of magnitude lower than for ILDM, implying that the RRM manifold is a better approximation for the SIM. As it can be seen from Fig. 3(b), the trajectory is attracted to the RRM manifold at  $(x, y) \simeq (0.4, 0.6)$ . At this location, the de-

fect of invariance for the RRM manifold is less than 0.03, while for ILDM it is approximately 0.6.

### III. CHEMICAL KINETICS

Consider a homogeneous mixture of ideal gases consisting of  $n_s$  species and  $n_e$  elements reacting under constant pressure  $p$  in a closed system. The number of moles are represented by the vector  $\mathbf{N} = (N_1, N_2, \dots, N_{n_s})^T$  and the change in the chemical composition of the species, results from  $r$  reversible reactions between the  $n_s$  reactants  $M_i$ ,



where  $v'_{ik}$  and  $v''_{ik}$  are the stoichiometric coefficients of species  $i$  in reaction  $k$  for the reactants and products, respectively. The rate of progress of reaction  $k$  is

$$q_k = k_{f_k} \prod_{i=1}^{n_s} [X_i]^{v'_{ik}} - k_{r_k} \prod_{i=1}^{n_s} [X_i]^{v''_{ik}}, \quad k = 1, \dots, r, \quad (13)$$

where  $[X_i]$  denotes the molar concentration of species  $i$  and  $k_{f_k}$  and  $k_{r_k}$  are the forward and reverse rate constants having the modified Arrhenius form

$$k_{f_k} = A_k T^{\beta_k} \exp\left(\frac{-E_k}{R_c T}\right), \quad (14)$$

with  $A_k$ ,  $\beta_k$ ,  $E_k$ , and  $R_c$  being the pre-exponential factor, temperature exponent, activation energy, and ideal gas constant, respectively. The forward and reverse rate constants are related via the equilibrium constant,  $K_{c_k}(T)$ ,

$$k_{r_k} = \frac{k_{f_k}}{K_{c_k}}. \quad (15)$$

The rate equation for species  $i$  is given by

$$\frac{d[X_i]}{dt} = \sum_{k=1}^r (v''_{ik} - v'_{ik}) q_k, \quad i = 1, \dots, n_s. \quad (16)$$

Using the reactor volume  $V$ , the change in the mole number of species  $i$  can be rewritten in the form of Eq. (1),

$$\frac{d\mathbf{N}}{dt} = \mathbf{f}(\mathbf{N}). \quad (17)$$

The  $n_e$  elemental conservation constraints can be expressed in terms of an  $n_e \times n_s$  elemental constraints matrix,  $\mathbf{E}$ , as<sup>25</sup>

$$\mathbf{E}\mathbf{N} = \boldsymbol{\xi}^e, \quad (18)$$

where  $\boldsymbol{\xi}^e$  is specified by the initial composition and  $E_{ji}$  denotes the number of atoms of element  $j$  in species  $i$ .

In a constant pressure adiabatic system the reactions proceed at constant enthalpy and the temperature evolution is governed by

$$\frac{dT}{dt} = -\frac{1}{\rho c_p} \sum_{i=1}^{n_s} h_i \dot{\omega}_i W_i,$$

where,  $\rho$  is the mixture density and  $W_i$ ,  $h_i$ , and  $\dot{\omega}_i$  are molecular weight, enthalpy and production/destruction rate of species  $i$ . According to the second law of thermodynamics, the system under consideration is equipped with a convex state function, the entropy  $S$ , which attains its global maximum at equilibrium. The negative of entropy, which for ideal gas mixtures under isobaric and isenthalpic conditions takes the form<sup>18</sup>

$$G = -S = -\frac{\sum_{i=1}^{n_s} X_i \left( s_i(T) - R_c \ln(X_i) - R_c \ln\left(\frac{p}{p_{ref}}\right) \right)}{\bar{W}} \quad (19)$$

is a thermodynamic Lyapunov function for the dynamics defined by (17) in terms of  $s_i$ , the specific entropy of species  $i$ ,  $\bar{W} = \sum_{i=1}^{n_s} X_i W_i$  the mean molecular weight,  $p$  and  $p_{ref}$  the system and reference pressures;  $X_i = N_i / \sum_{j=1}^{n_s} N_j$  is the mole fraction of species  $i$ .

The equilibrium composition,  $\mathbf{N}^{eq}$ , is the solution of the constrained minimization problem

$$\begin{aligned} \min \quad & G \\ \text{s.t.} \quad & \mathbf{E}\mathbf{N} = \boldsymbol{\xi}^e. \end{aligned} \quad (20)$$

This Lyapunov function can be exploited not only to compute the equilibrium but also for the derivation of the reduced description as described in Sec. IV.

#### IV. CONSTRUCTION OF THE REDUCED DESCRIPTION

The local realization of the Relaxation Redistribution Method<sup>18</sup> constructs and tabulates SIMs with dimension  $n_d$  adaptively varying in different regions of the phase space. Adaptation of the dimension is based on the failure of the algorithm to converge after a fixed number of iterations, which is taken as an indicator that the SIM dimension should be increased.

However, the computational cost associated with the manifold representation on a grid and the retrieval of information from high dimensional tables imposes restrictions on the dimensionality of the slow manifold, the target being a two- or three-dimensional table.<sup>4</sup> A low-dimensional SIM is usually limited to a small neighborhood of phase space around the equilibrium point, leaving open the problem of its extension to cover all admissible states.<sup>26</sup>

In this paper, the global realization of the RRM with an *a priori* chosen manifold dimension is employed. In particu-

lar, a RCCE manifold, which provides “good” manifolds as discussed in the Introduction, with dimension up to three is used to define the initial SIM. The initial approximation is subsequently refined using RRM. For regions of the phase space in the neighborhood of the equilibrium, the method converges to the SIM. For states farther away, where no SIM with the chosen dimension exists, the refined Quasi-Equilibrium Manifold (QEM) defined below provides an accurate extension as will be shown in Sec. V. In addition to the parametrization of the SIM, the initial RCCE manifold defines the boundaries which are kept fixed during the application of RRM.

#### A. Initialization: The quasi-equilibrium manifold

For systems equipped with a Lyapunov function, a reduced description can be obtained based on the notion of the QEM<sup>1</sup> (known as Constrained Equilibrium Manifold (CEM) in the combustion literature<sup>9,10</sup>). QEM assumes that the system relaxes to equilibrium through a sequence of quasi-equilibrium states at a rate controlled by a set of appropriate slowly-varying constraints  $\boldsymbol{\xi}$ .<sup>1,9,10,27</sup> Since the Lyapunov function  $G$  decreases in time, a QEM can be interpreted as the constrained minimum of  $G$ .

In addition to the elemental conservation constraints (Eq. (18)), QEM imposes *a priori*  $n_d$  linear constraints on the system state defining the slow macroscopic variables

$$\boldsymbol{\xi}^d = (\mathbf{B}^d)\mathbf{N}, \quad (21)$$

where  $\mathbf{B}^d$  is an  $n_d \times n_s$  matrix with rows obtained from the coefficients of the linear combinations of the number of moles providing the  $n_d$  slow parametrizing variables  $\boldsymbol{\xi}^d$ . Thus, the total number of constraints amounts to  $n_c = n_e + n_d$ , and the QEM is the map  $\mathbf{N}^{\text{QEM}}(\boldsymbol{\xi})$ , obtained by solving the following constrained convex minimization problem:

$$\begin{aligned} \min \quad & G, \\ \text{s.t.} \quad & \mathbf{B}\mathbf{N} = \boldsymbol{\xi}. \end{aligned} \quad (22)$$

Here,  $\mathbf{B} = [\mathbf{E}\mathbf{B}^d]$  is the  $n_c \times n_s$  constraint matrix and  $\boldsymbol{\xi} = [\boldsymbol{\xi}^e \boldsymbol{\xi}^d]$  the constraint vector with  $n_c$  elements. The  $n_s$ -dimensional state  $\mathbf{N}$  can then be parametrized by the  $n_c$  variables  $\boldsymbol{\xi}$ . For model reduction purposes,  $n_c \ll n_s$ .

In closed reactive systems, the elemental mole numbers must be conserved. Hence,  $\mathbf{E}\mathbf{N} = \boldsymbol{\xi}^e$  is fixed upon definition of the fresh mixture condition. The constraint matrix  $\mathbf{B}^d$  can be selected on the basis of numerical results of detailed solutions for similar problems, as suggested, for example, in Ref. 28. Alternatively, a suitable parametrization can be extracted using the spectral decomposition of the Jacobian matrix evaluated at the equilibrium point.<sup>29</sup> It should be pointed out that a QEM is typically neither an invariant nor a slow manifold.<sup>27</sup>

The choice of a good set of constraints can be challenging. In addition to intuition and the mentioned approaches, CSP analysis of detailed simulations can aid in the selection.<sup>28</sup> The Level Of Importance (LOI), which finds the species associated with the short time scales by means of a combined species lifetime and sensitivity parameters, has also been used in the RCCE context.<sup>30</sup>

TABLE I. Matrix  $B^d$  for the  $H_2$ /air mixture.

Reduced variable	$H_2$	$N_2$	H	O	OH	$O_2$	$H_2O$	$HO_2$	$H_2O_2$
$\xi_1^d = \text{TM}$	1	1	1	1	1	1	1	1	1
$\xi_2^d = \text{AV}$	0	0	1	2	1	0	0	0	0
$\xi_3^d = \text{FO}$	0	0	0	1	1	0	1	0	0

The RCCE method, which is based on the QEM approach can be used either as proposed originally,<sup>31–33</sup> or in combination with other methods.<sup>34</sup> The most commonly employed slowly-changing constraints are the total number of moles (TM), the total number of radicals referred to active valence (AV), and free oxygen (FO), which refers to the reactions where the O–O bond is broken.<sup>27</sup> These RCCE linear constraints for hydrogen/air combustion are specified in Table I. The RCCE manifold is unique and infinitely differentiable, and can be used even for states far from equilibrium.<sup>25,35</sup> In this paper, we exploit the QEM notion only to construct the initial approximation of the SIM and to define the manifold boundaries.

## B. The global relaxation redistribution algorithm

As discussed in Sec. II, the boundaries of the initial grid shrink during relaxation. In the local RRM, reconstruction of the boundary points by re-stretching the relaxed grid to the fixed boundaries is done by linear extrapolation. However, such an approach cannot always guarantee physically meaningful values for the species concentrations. In order to avoid these difficulties, the boundary of the SIM can be fixed to the initial guess provided by the QEM, and the RRM procedure is applied only to the interior grid points.

The embarrassingly simple steps for the computation of the global manifold proceed as follows:

1. Choose the manifold dimension  $n_d$  and select the parametrizing variables  $\xi_i$ .
2. Construct the  $n_d$ -dimensional QEM,  $\mathbf{N}^{\text{QEM}}(\xi^d)$ , by solving the minimization problem (22). This manifold corresponds to constructing the initial grid indicated by the solid line with filled circles in Fig. 1(b).
3. Fix the grid boundaries to the boundaries of QEM.
4. Relax the interior grid nodes by integrating

$$\frac{d\mathbf{N}}{dt} = \mathbf{f}(\mathbf{N}^{\text{QEM}}(\xi^d)) \quad (23)$$

for a fixed time step  $\Delta t$  to obtain  $\mathbf{N}^{\text{relax}}$ . As shown schematically in Fig. 1(b) (filled circles relaxing towards the open circles), this equation expresses the temporal evolution of composition confined onto the SIM. The new locations of the relaxed nodes in the manifold parametrization space  $\Xi$  are then obtained from

$$\xi_r^d = (\mathbf{B}^d)\mathbf{N}^{\text{relax}}. \quad (24)$$

5. Redistribute the grid nodes back to the original locations in the manifold parametrization space

$$\mathbf{N}^{\text{relax}}(\xi_r^d) \rightarrow \mathbf{N}^{\text{RRM}}(\xi^d) \quad (25)$$

using interpolation through the scattered relaxed nodes. This is similar to finding the filled squares in Fig. 1(b), with the difference that boundaries are fixed and there is no extrapolation between the relaxed nodes.

6. Repeat steps 4–5 until the grid points do not change appreciably.

It should be pointed out that the reduced descriptions obtained by this algorithm are closely related to the ICE-PIC approach suggested by Ren *et al.* in Ref. 11, as both procedures construct invariant manifolds forced to pass by the same boundary points (QEM boundary points).

## C. Rate equations for the slow variables

Once the slow invariant manifold is constructed, the temporal evolution of the reduced system along the SIM can be recast in the following general form in terms of the macroscopic slow variables  $\xi^d$  chosen to parametrize the SIM:

$$\frac{d\xi^d}{dt} = (\mathbf{B}^d)\mathbf{P}\mathbf{f}(\mathbf{N}^{\text{RRM}}(\xi^d)). \quad (26)$$

If the slow invariant manifold is known with high accuracy, the vector field  $\mathbf{f}$  is perfectly aligned with the manifold's tangent space and the state would never depart from the manifold. In most computational applications of practical interest, however, SIM approximations with different levels of accuracy are employed, and the chosen parametrization cannot completely decouple the fast and slow components. In these cases,  $(\mathbf{B}^d)\mathbf{f}$  does not lie on the tangent space of the SIM and a projector  $\mathbf{P}$  is needed to bring the state back to the manifold.

Different projectors have been proposed in the literature. The ILDM projector recovers the fast subspace to leading order, and the kernel of the projector is constructed using the fastest eigenvectors of the local Jacobian. Higher order approximations can be constructed using the CSP basis vectors. Details on the ILDM and CSP projectors can be found in Refs. 6 and 7. Another option for  $\mathbf{P}$  is the thermodynamic projector,<sup>36</sup> which can be constructed on the basis of the local tangent space to the SIM and the derivatives of a thermodynamic Lyapunov function (19).<sup>37</sup>

In the classical RCCE method, it is assumed that states of the system always remain on the QEM and the rate equations for the slow parametrizing variables is close to the tangent space of the manifold.<sup>27</sup> The  $n_s$ -dimensional composition space is decomposed into the  $n_d$ -dimensional *represented* subspace spanned by the rows of  $\mathbf{B}^d$  and its orthogonal complement, the *unrepresented* subspace of dimension  $n_s - n_d$ . The projection matrix then becomes the  $n_s \times n_s$ -dimensional identity matrix which implies that the rate of change in the unrepresented subspace is negligible. Therefore, we rely upon the fact that fast motions are expected to mostly occur in the null space of the  $\mathbf{B}^d$  matrix. For a more detailed analysis of this projector see Ref. 38. The same approach was used in the applications of Sec. V.

The following steps describe the implementation of reduced chemistry in a reacting flow simulation: (a) From the specified composition at time  $t_n$ ,  $\mathbf{N}_n = \mathbf{N}(t_n)$ , and the

thermodynamic conditions, the values for the parametrizing variables can be found using Eq. (21),

$$(\mathbf{B}^d)\mathbf{N}_n = \xi_n^d. \quad (27)$$

(b) The rate equations (26) for  $\xi^d$ , are advanced in time to find  $\xi_{n+1}^d$ , where  $\mathbf{N}_n^{RRM}$  are the projected values of  $\mathbf{N}(t_n)$  on the SIM.

The reduced model can be tabulated in terms of either the reduced state  $\mathbf{N}^{RRM}$  or of the projected right hand side of the evolution equations  $(\mathbf{B}^d)f(\mathbf{N}^{RRM})$ . In the former case, interpolation of the tabulated data is used to retrieve the composition vector corresponding to  $\xi_{n+1}^d$ . In the latter, the right hand side of (26) is obtained directly to proceed with the integration of the reduced system and the compositions can be obtained separately in a post-processing step.

The overall computational cost for the integration of the full system of  $n_s$  differential equations is thus replaced by the cost of integrating  $n_d$  differential equations and of interpolation. The following practical issues should be pointed out: (i) Choosing the appropriate constraints with respect to the initial composition is important. The kernel of  $\mathbf{B}^d$  should not be spanned by the  $f(\mathbf{N}_n^{RRM}(\xi^d))$  vector, since in that case  $\frac{d\xi^d}{dt}$  becomes zero and there is no temporal evolution of  $\xi^d$ ; (ii) Interpolation can affect the result strongly as shown in Ref. 39. This effect can be controlled by refining the table and/or using appropriate interpolation methods, albeit at higher computational cost; (iii) By construction, the approach presented here guarantees that the equilibrium will be accurately captured by the reduced description. This appears to not always be the case with reduced mechanisms proposed in the literature; (iv) In problems like the ignition delay time considered in Sec. V, the projection of the initial state on the manifold is crucial for the comparison with the prediction of the detailed reaction mechanism. In the literature, the comparison is often made by taking the initial state to lie *on* the manifold. In the auto-ignition validation of Sec. V good results are obtained by comparing the detailed solution with those obtained by projecting the initial state on the manifold using the constrained equilibrium assumption.

## V. VALIDATION AND DISCUSSION

### A. Auto-ignition of homogeneous mixtures

The global RRM method is applied to a homogeneous  $\text{H}_2/\text{air}$  mixture using the detailed reaction mechanism of Li *et al.*<sup>40</sup> ( $n_s = 9$  species and 21 reactions) at atmospheric pressure and different initial temperatures  $T_0$ .

The initial reactant composition is that of a stoichiometric mixture ( $N_{\text{H}_2}^0 = 1.0$ ,  $N_{\text{O}_2}^0 = 0.5$ , and  $N_{\text{N}_2}^0 = 1.881$  mole), while the remaining species are assigned the chemically insignificant positive values  $N = 10^{-12}$  mole to ensure strictly positive species compositions at the constrained equilibrium state and guarantee the existence and uniqueness of the solution to the minimization problem (22).<sup>27</sup> The equilibrium point (steady state) can be computed by minimizing the Gibbs function under constant pressure and enthalpy. Then, the initial and equilibrium states are projected on the mani-

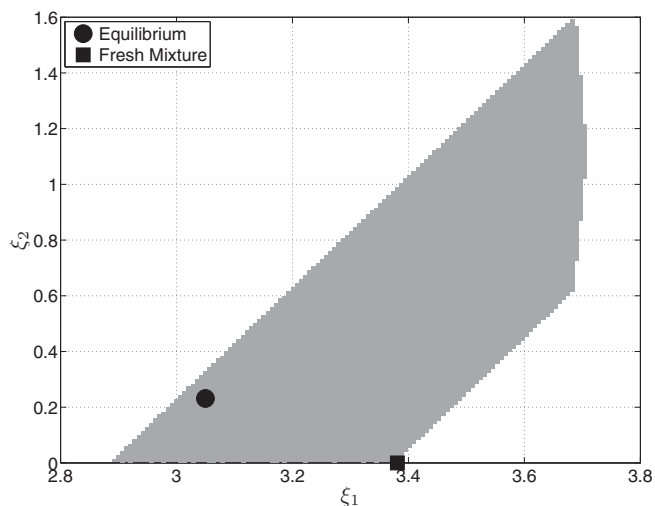


FIG. 4. Projection of manifold (grid) onto  $\Xi$ . The initial grid should contain both the fresh mixture and equilibrium point, and extend in the manifold parametrization space as far as the QEM convex minimization calculations converge.

fold parametrization space,  $\Xi$ , using (21). Different combinations of constraints for hydrogen combustion have been investigated in the literature.<sup>27,35</sup> The TM and AV constraints (Table I) have been found to give better agreement with respect to ignition delay times for a wide range of thermodynamic conditions and are chosen for the  $\xi$  parameterization. Starting from a sufficiently large range in the parametrization space that contains the initial and steady states, the CEQ code<sup>41,42</sup> is used for the construction of the RCCE-based initial manifold as discussed in Sec. IV B. The code computes the constrained equilibrium state by minimizing the Gibbs function under fixed pressure and enthalpy; the projection of the computed initial manifold on  $\Xi$  is shown in Fig. 4.

The boundary nodes are then fixed, and the RRM procedure is applied to the interior nodes. For the redistribution step, the linear Shepard method implemented in the SHEPPACK package<sup>43</sup> is used for interpolation,

$$\mathbf{N}^{RRM}(\xi^d) = \frac{\sum_{k=1}^{n_{gp}} \alpha_k(\xi^d) \mathbf{N}^{relax}(\xi_r^d)}{\sum_{k=1}^{n_{gp}} \alpha_k(\xi^d)}, \quad (28)$$

where  $n_{gp}$  is the total number of grid points and the weights  $\alpha_k(\xi^d)$  are defined as

$$\alpha_k(\xi^d) = \frac{1}{\|\xi^d - \xi_r^{d(k)}\|_2^2}. \quad (29)$$

For initial temperature  $T_0 = 1500$  K, the two-dimensional RCCE and global RRM manifolds for selected species are plotted in Fig. 5 together with the trajectory obtained using the detailed mechanism (thick solid line). For the major species, the global RRM manifold brings only a slight improvement over the RCCE manifold, while for  $\text{HO}_2$  and  $\text{H}_2\text{O}_2$  the improvement is significant. As it can be seen in Fig. 5, the RCCE manifold is not invariant. This is more clearly seen in the temporal evolution of the temperature and species mass fractions, plotted in Fig. 6. Good agreement is found with the detailed description for the temperature and major reactants as

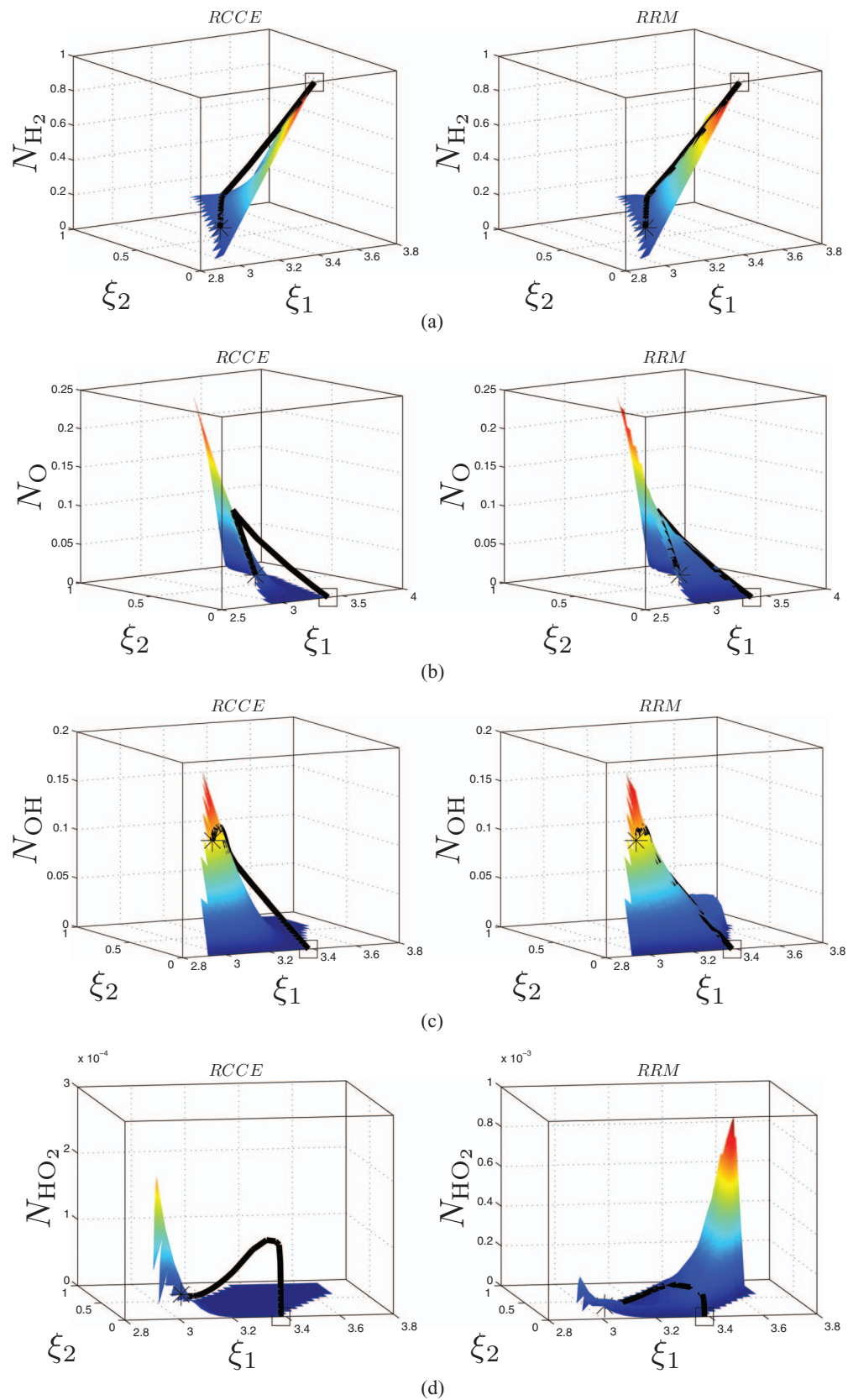


FIG. 5. (a)–(d) Comparison of the RCCE (left column) and RRM (right column) manifolds for  $T_0 = 1500$  K. ( $\square$ : fresh mixture;  $\star$ : equilibrium point;  $-$ : detailed kinetics trajectory).

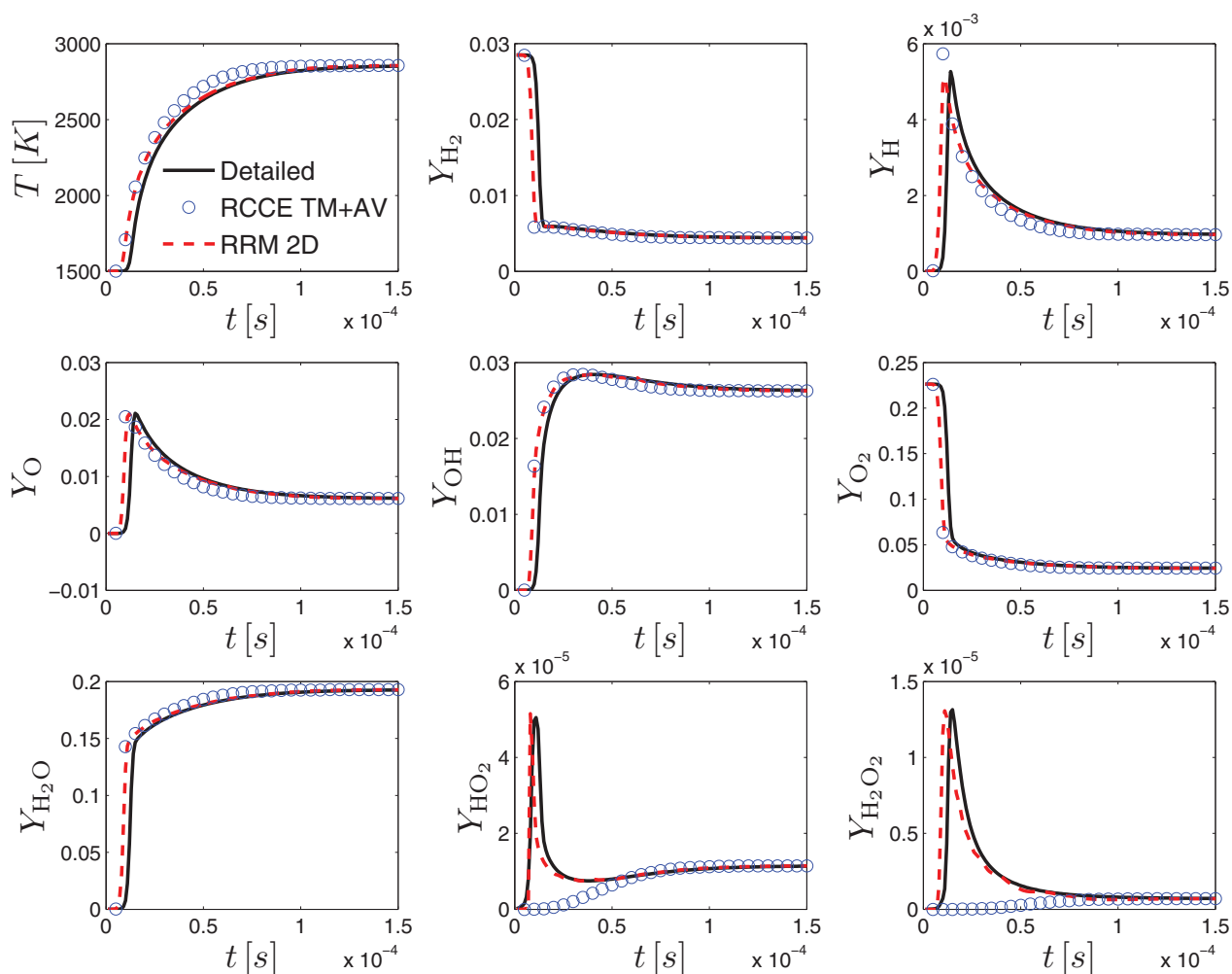


FIG. 6. Time histories of the temperature and species mass fractions for  $\text{H}_2/\text{air}$  autoignition with unburnt temperature  $T_0 = 1500 \text{ K}$ .

well as the radicals with high enough concentration. Far away from equilibrium, the RCCE manifold strongly underpredicts the concentration of  $\text{HO}_2$  and  $\text{H}_2\text{O}_2$ . The time history of the weighted root mean square norm as used for error estimation in Ref. 44 of the defect of invariance vector is plotted in Fig. 7 together with the temperature profiles computed using the detailed and reduced descriptions. After  $40 \mu\text{s}$ , the defect drops below  $10^{-4}$  and the detailed and reduced models are in good agreement. This illustrates that the defect of invariance is a convenient indicator of the accuracy of the reduced description. During the initial transient, a higher-dimensional manifold should be used.

The number of right hand side function evaluations  $n_{\text{fe}}$  during integration can be used as an indicator for the stiffness. Figure 8 shows the temperature and  $n_{\text{fe}}$  obtained by using the stiff ODE integrator DVODE<sup>44</sup> with an output time step  $\delta t = 10^{-5}$  (the integrator adapts the time step during integration from time  $t$  to  $t + dt$ ). The initial composition for the detailed mechanism was the stoichiometric mixture, while for the reduced description its projection on the RRM manifold was used. With the exception of a single time instant close to ignition,  $n_{\text{fe}}$  is lower for the reduced model during the whole integration interval.

At a lower initial temperature  $T_0 = 1000 \text{ K}$ , the 2D manifold can no longer provide an accurate reduced description (Fig. 9). The construction of a 3D slow manifold is straightforward starting from an initial manifold constructed using all constraints of Table I. The results obtained with RCCE with two (open squares) and three (open circles) constraints, the RRM 2D (dotted-dashed line) and 3D (dashed line) manifolds are compared with the detailed evolution (solid line) in Fig. 9. While the 3D RCCE manifold results in small improvement, the increase in the manifold dimension of the RRM manifold leads to very good agreement with respect to the prediction accuracy of the ignition delay time and the temporal evolution of temperature and species, with the exception of the  $Y_{\text{H}_2\text{O}_2}$  profile which displays a noticeable deviation from the detailed mechanism profile. The ignition delay times,  $\tau_{\text{ig}}$ , defined as the time corresponding to the inflection point of the temperature profile are summarized in Table II.

The magnitude of the real part of the six non-trivial eigenvalues of the Jacobian matrix during the temporal evolution for  $T_0 = 1000 \text{ K}$  and  $T_0 = 1500 \text{ K}$  are reported in Fig. 10. The absolute value of the inverse of the eigenvalues determine the time scales of the chemical modes and the ratio  $\lambda_i/\lambda_s$  of the most to the less negative eigenvalues is an

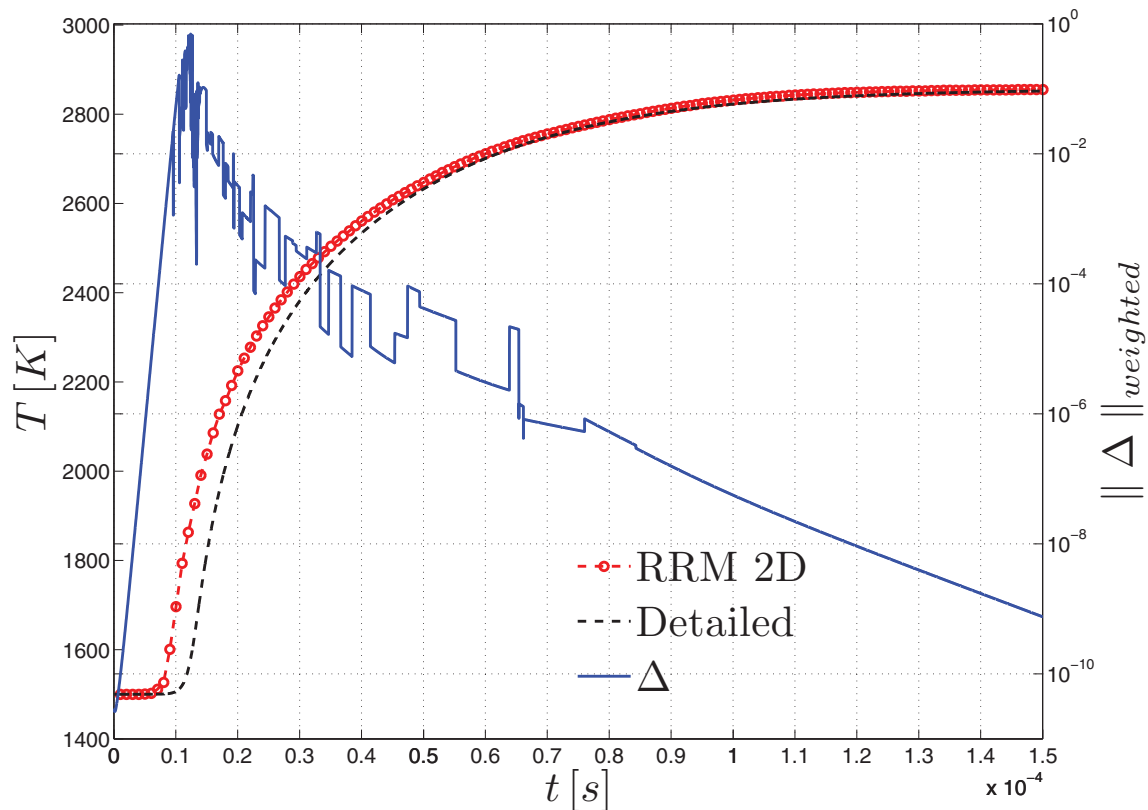


FIG. 7. Comparison of the temperature profiles obtained with the detailed and the reduced 2D RRM description and evolution of the norm of the defect of invariance for  $T_0 = 1500$  K.

estimation for the stiffness. For  $T_0 = 1000$  K, the gap is  $\lambda_f/\lambda_s \simeq 8.5 \times 10^8$ , while for  $T_0 = 1500$  K the ratio becomes  $\lambda_f/\lambda_s \simeq 5.6 \times 10^5$ , reflecting the higher stiffness at lower temperatures. In addition, if time scales  $1/|\lambda|$  shorter than  $10^{-4}$  [s] are considered as fast, the initial slow subspace of the  $T_0 = 1000$  K case is three dimensional while, for  $T_0 = 1500$  K, a

2D slow manifold can be used. Eigenvalues with positive real part indicating explosive behavior were found initially in both cases and time intervals where the eigenvalues cross and become complex pairs were observed during the evolution from the initial to the equilibrium state. Manifolds of higher dimensions would be needed to capture more accurately the reduced dynamics in these intervals, as was done in the adaptive version of RRM.<sup>18</sup> Careful examination of Fig. 10 for  $T_0 = 1500$  K reveals that eigenvalue crossings correspond to jumps in (a) the defect of invariance vector (Fig. 7) and (b) the number of source term evaluations  $n_{fe}$  (Fig. 8). The effect of eigenvalues crossing on the quality of reduced model is discussed in Ref. 45. It nevertheless appears that these short intervals do not affect the quality of the manifold significantly.

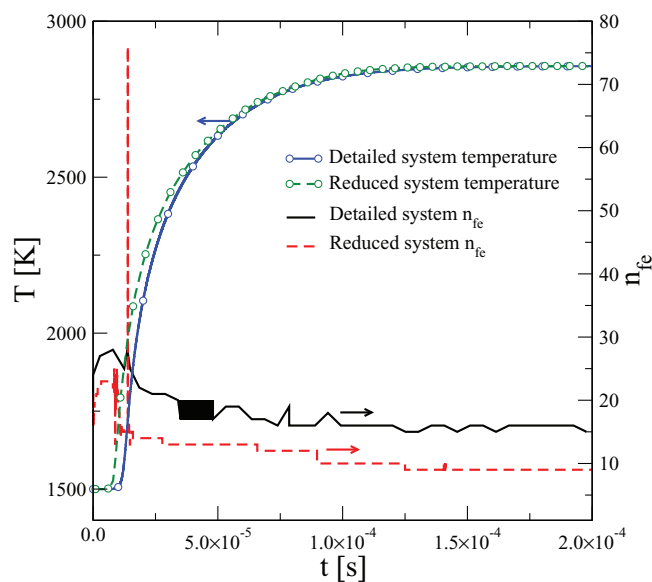


FIG. 8. Comparison of temperature evolution and number of source term evaluations  $n_{fe}$  obtained with the detailed mechanism and the reduced 2D RRM description at  $T_0 = 1500$  K.

## B. Premixed laminar flame

The steady, atmospheric, adiabatic, one-dimensional laminar premixed flame of a stoichiometric hydrogen/air mixture and multi-component transport properties was considered in order to study the ability of the 2D RRM manifold constructed from the homogeneous auto-ignition of an unburnt mixture at  $T_u = 700$  K to reconstruct the unrepresented variables in a case where transport phenomena play a dominant role. A similar procedure was used for the validation of the ICE-PIC manifold by Ren *et al.*<sup>11</sup>

In this case, the manifold parametrization becomes important since in the general case of non-unity Lewis numbers it is difficult to solve the partial differential equations even

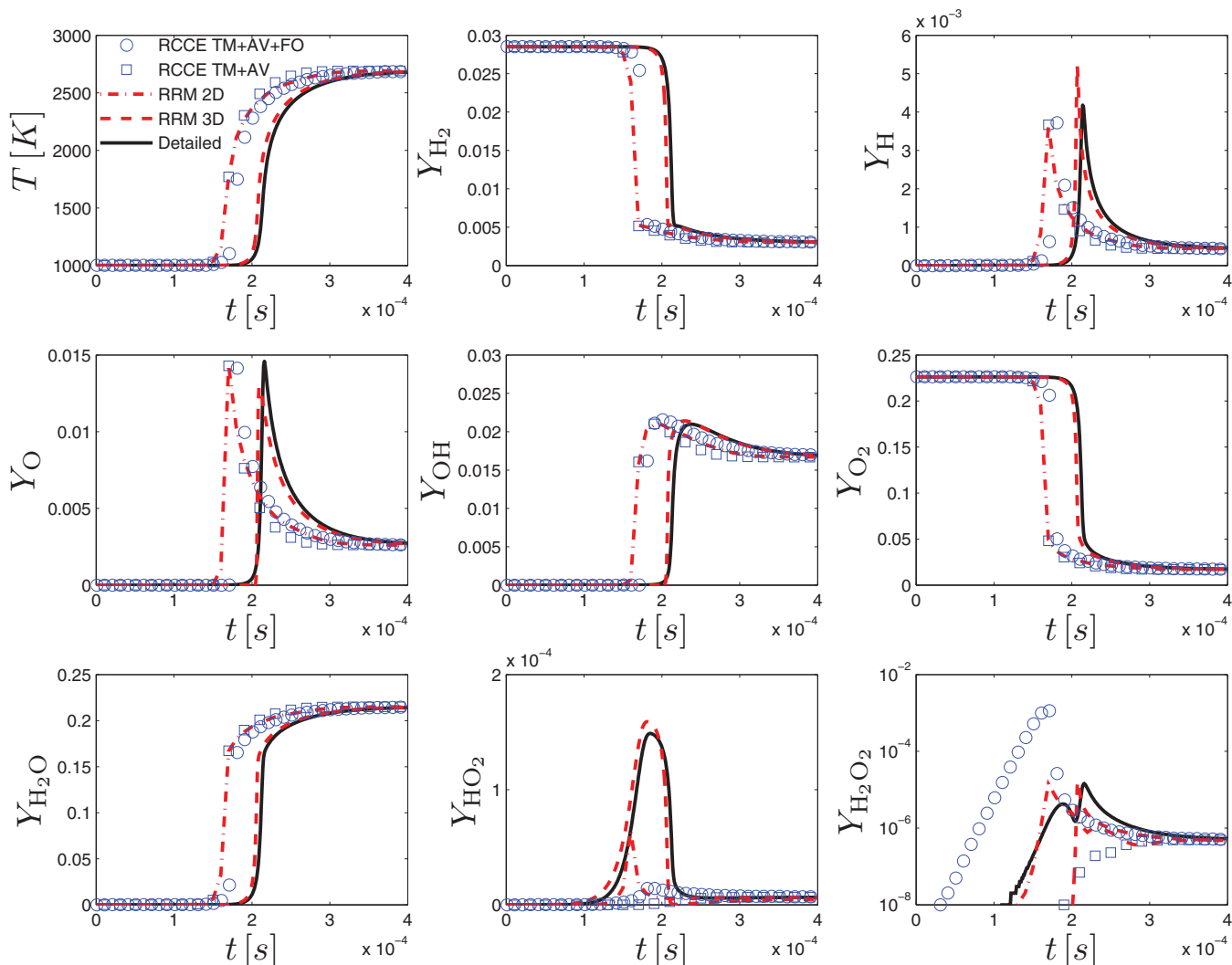


FIG. 9. Temperature and species mass fractions as the function of time for  $\text{H}_2/\text{air}$  auto-ignition,  $T_0 = 1000$  K. Detailed, RCCE with 2 Constraints, RCCE with 3 Constraints, RRM 2D manifold, RRM 3D manifold are compared.

when the parametrizing variables are linear combinations of the original variables.<sup>46</sup> Here, the quasi-equilibrium manifold was constructed using the mole fractions of  $\text{H}_2\text{O}$  and  $\text{H}_2$  as slow constraints ( $\xi_1 = X_{\text{H}_2\text{O}}$  and  $\xi_2 = X_{\text{H}_2}$ ). The RRM refinement process was applied starting from the QEM to find the global two-dimensional manifold for  $T_u = 700$  K. The species concentrations as a function of the distance,  $x$ , is computed using PREMIX from the CHEMKIN application suite.<sup>47</sup> The local values of  $X_{\text{H}_2}$  and  $X_{\text{H}_2\text{O}}$  from the detailed chemistry 1D flame structure were used to reconstruct the remaining species using the RRM manifold.

TABLE II. Comparison of ignition delay times deduced from detailed and reduced models.

Method	$\tau_{ig}$ (s)
Detailed	0.000213
RCCE TM+AV	0.000169
RCCE TM+AV+FO	0.000178
RRM 2D	0.000170
RRM 3D	0.000207

The agreement for the major species and temperature between the detailed solution and the reconstruction is excellent (Fig. 11). The largest differences are observed for the  $\text{H}_2\text{O}_2$  radical and they can be mainly attributed to the incorrectly predicted value of QEM at the “cold” (unburned mixture) boundary. In addition to low dimensionality effects, molecular diffusion in laminar flames can drive the compositions away from the manifold, potentially contributing in the differences observed in the O and H radicals profiles. Similar observations are reported in the literature, where different methods of projecting the diffusion term onto the manifold were studied (see, for example, Refs. 48 and 49).

## VI. CONCLUSIONS

In this paper, we presented an algorithm based on the RRM for the construction of the SIM of an *a priori* chosen dimension which covers a large fraction of the admissible composition space that includes the equilibrium as well as the initial state.

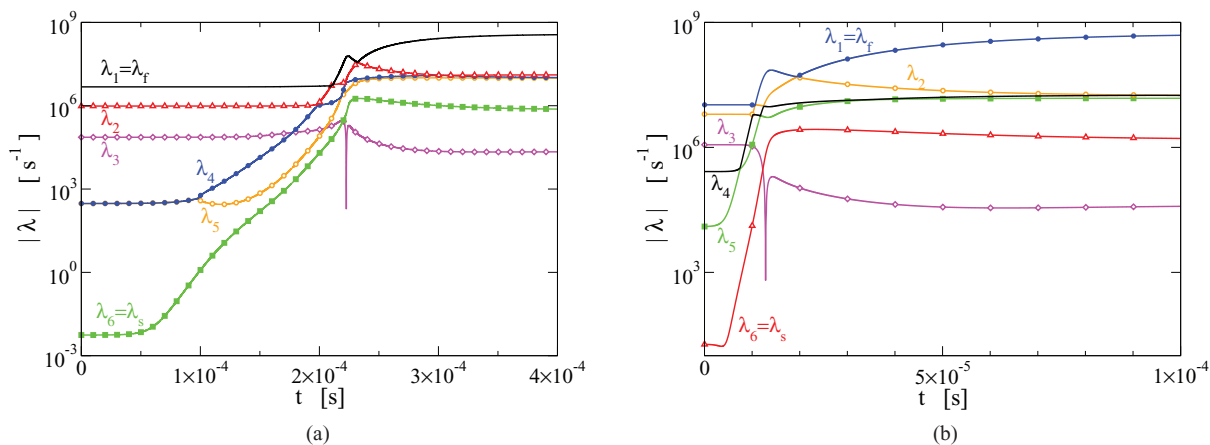


FIG. 10. Temporal evolution of the six non-trivial eigenvalues of the Jacobian along the solution trajectory: (a)  $T_0 = 1000$  K, (b)  $T_0 = 1500$  K.

The manifold parametrization and boundaries are determined with the help of the RCCE method, which also provides the initial guess for the SIM. The guess is iteratively refined and the converged manifold is tabulated. The method

is easy to implement and robust to use for the construction of reduced manifolds of high dimensionality, which were found to be invariant over extended regions of the admissible space. A criterion based on the departure from invariance is proposed

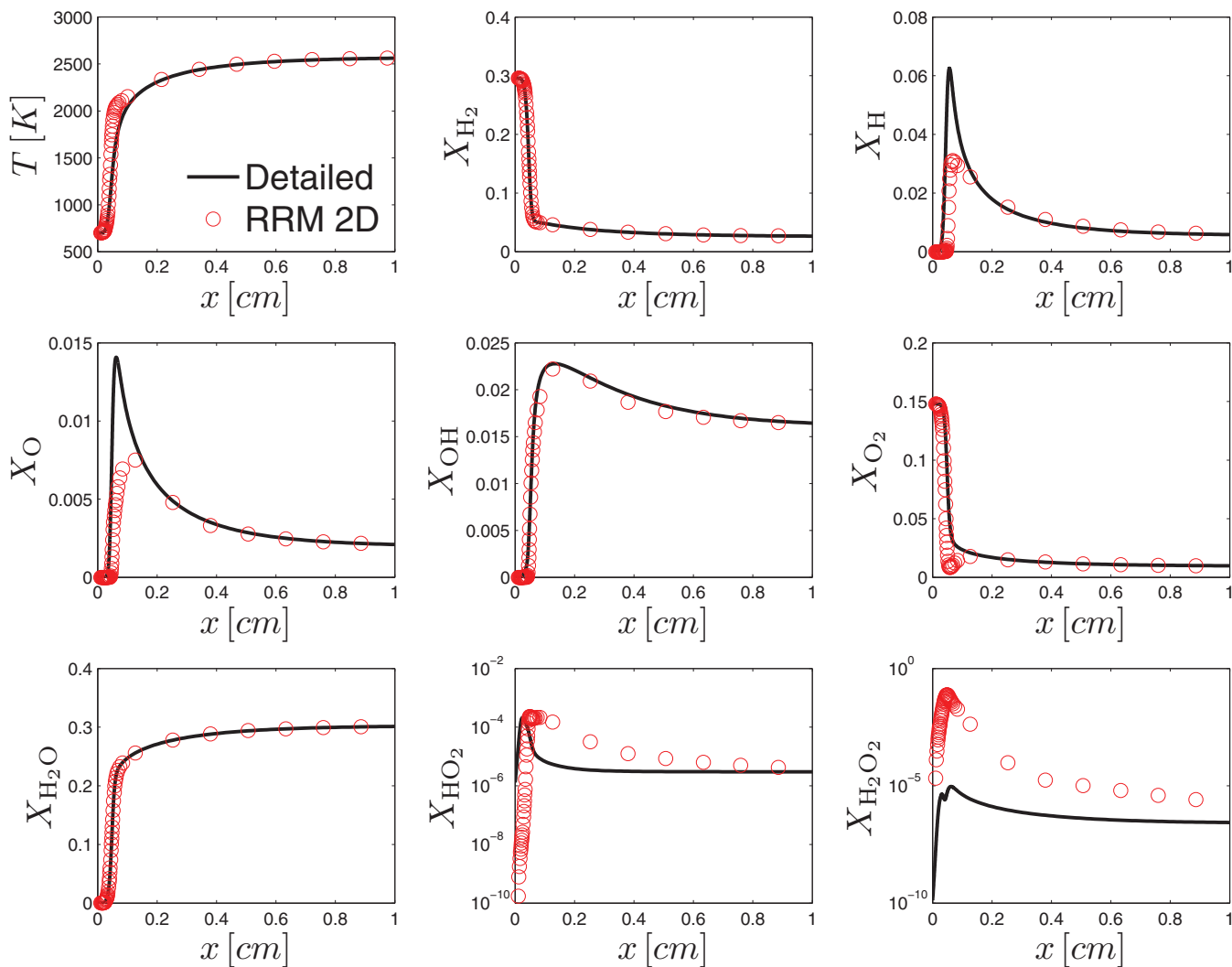


FIG. 11. Comparison of the temperature and species mole fractions profiles computed by PREMIX (lines) and reconstructed using the 2D RRM manifold (symbols) for unburnt mixture at  $T_0 = 700$  K.

to find the region over which the reduced description is valid. The accuracy of the method was assessed by comparing trajectories for auto-ignition calculations of homogeneous H<sub>2</sub>/air mixtures at different initial temperatures  $T_0$ . At  $T_0 = 1500$  K, a 2D manifold is found to capture accurately both the ignition delay time and the temporal evolution of all the species and shows significant improvement with respect to the low concentration species (HO<sub>2</sub> and H<sub>2</sub>O<sub>2</sub>) compared to a RCCE manifold. At  $T_0 = 1000$  K, a 3D manifold is needed to reproduce accurately the detailed dynamics with the exception of the pre-ignition profiles of H<sub>2</sub>O<sub>2</sub>.

The significant reduction in the number of source term evaluations indicates that the reduced descriptions are less stiff. However, similar to all other reduction methods based on tabulation, fast table searching, and interpolation algorithms are essential for the overall efficiency of the reduced scheme.

The 2D RRM manifold can reconstruct the laminar premixed flame structure fairly accurately compared with the results obtained with the detailed mechanism, indicating that it can be used in multidimensional simulations where transport properties play a dominant role.

## ACKNOWLEDGMENTS

Financial support of the Swiss National Science Foundation under Project No. 137771 is gratefully acknowledged. I.V.K. gratefully acknowledges support by the European Research Council (ERC) Advanced Grant No. 291094-ELBM; E. Chiavazzo thanks the support by the Fulbright commission.

- <sup>1</sup>A. N. Gorban and I. V. Karlin, *Invariant Manifolds for Physical and Chemical Kinetics*, Lecture Notes in Physics Vol. 660 (Springer, 2005).
- <sup>2</sup>C. K. Law, *Combustion Physics* (Cambridge University Press, 2006).
- <sup>3</sup>D. A. Goussis and U. A. Maas, in *Turbulent Combustion Modeling*, Fluid Mechanics and Its Applications Vol. 95, edited by T. Echehki and E. Mastorakos (Springer, 2011), pp. 193–220.
- <sup>4</sup>S. B. Pope, *Proc. Combust. Inst.* **34**, 1 (2013).
- <sup>5</sup>A. N. Al-Khateeb, J. M. Powers, S. Paolucci, A. J. Sommes, J. A. Diller, J. D. Hauenstein, and J. D. Mengers, *J. Chem. Phys.* **131**, 024118 (2009).
- <sup>6</sup>S. H. Lam and D. A. Goussis, *Proc. Combust. Inst.* **22**, 931 (1989).
- <sup>7</sup>U. Maas and S. B. Pope, *Combust. Flame* **88**, 239 (1992).
- <sup>8</sup>H. G. Kaper and T. J. Kaper, *Physica D* **165**, 66 (2002).
- <sup>9</sup>J. C. Keck and D. Gillespie, *Combust. Flame* **17**, 237 (1971).
- <sup>10</sup>J. C. Keck, *Progr. Energy Combust. Sci.* **16**, 125 (1990).
- <sup>11</sup>Z. Ren, S. B. Pope, A. Vladimirovsky, and J. M. Guckenheimer, *J. Chem. Phys.* **124**(11), 114111 (2006).
- <sup>12</sup>D. Lebiez, *J. Chem. Phys.* **120**, 6890 (2004).
- <sup>13</sup>M. R. Roussel and S. J. Fraser, *J. Chem. Phys.* **94**, 7106 (1991).

- <sup>14</sup>J. Mengers and J. M. Powers, *SIAM J. Appl. Dyn. Syst.* **12**, 560 (2013).
- <sup>15</sup>D. Lebiez, J. Siehr, and J. Unger, *SIAM J. Sci. Comput.* **33**, 703 (2011).
- <sup>16</sup>D. Lebiez and J. Siehr, *Flow Turbul. Combust.* **92**, 885 (2014).
- <sup>17</sup>A. N. Gorban, I. V. Karlin, and A. Y. Zinovyev, *Physica A* **333**, 106 (2004).
- <sup>18</sup>E. Chiavazzo and I. V. Karlin, *Phys. Rev. E* **83**, 036706 (2011).
- <sup>19</sup>A. Debussche and R. Temam, *Appl. Math. Lett.* **4**, 73 (1991).
- <sup>20</sup>J. C. Robinson, *Phys. Lett. A* **200**, 415 (1995).
- <sup>21</sup>A. N. Gorban and I. V. Karlin, *Physica A* **190**, 393 (1992).
- <sup>22</sup>A. C. Tsoumanis, K. Rajendran, C. I. Siettos, and I. G. Kevrekidis, *New J. Phys.* **14**, 083037 (2012).
- <sup>23</sup>A. N. Gorban and I. V. Karlin, *Chem. Eng. Sci.* **58**, 4751 (2003).
- <sup>24</sup>V. Bykov, I. Goldfarb, V. Gol'dstein, and U. Maas, *IMA J. App. Math.* **71**, 359 (2006).
- <sup>25</sup>S. B. Pope, *Combust. Flame* **139**, 222 (2004).
- <sup>26</sup>V. Bykov and U. Maas, *Proc. Combust. Inst.* **31**, 465 (2007).
- <sup>27</sup>Q. Tang and S. B. Pope, *Combust. Theory Model.* **8**, 255 (2004).
- <sup>28</sup>W. P. Jones and S. Rigopoulos, *Combust. Flame* **142**, 223 (2005).
- <sup>29</sup>E. Chiavazzo, A. N. Gorban, and I. V. Karlin, *Commun. Comput. Phys.* **2**, 964 (2007).
- <sup>30</sup>S. Rigopoulos and T. Løvås, *Proc. Combust. Inst.* **32**, 569 (2009).
- <sup>31</sup>P. Bishnu, D. Hamiroune, M. Metghalchi, and J. C. Keck, *Combust. Theory Model.* **1**, 295 (1997).
- <sup>32</sup>D. Hamiroune, P. Bishnu, M. Metghalchi, and J. C. Keck, *Combust. Theory Model.* **2**, 81 (1998).
- <sup>33</sup>M. Janbozorgi, S. Ugarte, H. Metghalchi, and J. C. Keck, *Combust. Flame* **156**, 1871 (2009).
- <sup>34</sup>V. Hiremath, S. Lantz, H. Wang, and S. B. Pope, *Proc. Combust. Inst.* **34**, 205 (2013).
- <sup>35</sup>R. Law, M. Metghalchi, and J. C. Keck, *Proc. Combust. Inst.* **22**, 1705 (1989).
- <sup>36</sup>A. N. Gorban and I. V. Karlin, *Phys. A* **336**, 391 (2004).
- <sup>37</sup>E. Chiavazzo, I. V. Karlin, and A. N. Gorban, *Commun. Comput. Phys.* **8**, 701 (2010).
- <sup>38</sup>V. Hiremath and S. B. Pope, *Combust. Theory Model.* **17**, 260 (2013).
- <sup>39</sup>D. Schmidt, J. Segatz, U. Riedel, J. Warnatz, and U. Maas, *Combust. Sci. Technol.* **113**, 3 (1996).
- <sup>40</sup>J. Li, Z. Zhao, A. Kazakov, and F. L. Dryer, *Int. J. Chem. Kin.* **36**, 566 (2004).
- <sup>41</sup>S. B. Pope, “The computation of constrained and unconstrained equilibrium compositions of ideal gas mixtures using gibbs function continuation,” Report No. FDA03-02, Cornell University, 2003, see [http://eccentric.mae.cornell.edu/~pope/Reports/CEQ\\_FDA.pdf](http://eccentric.mae.cornell.edu/~pope/Reports/CEQ_FDA.pdf).
- <sup>42</sup>S. B. Pope, CEQ: A Fortran library to compute equilibrium compositions using gibbs function continuation, 2003.
- <sup>43</sup>W. I. Thacker, J. Zhang, L. T. Watson, J. B. Birch, M. A. Iyer, and M. W. Berry, *ACM Trans. Math. Soft. (TOMS)* **37**, 34 (2010).
- <sup>44</sup>P. N. Brown, G. D. Byrne, and A. C. Hindmarsh, *SIAM J. Sci. Stat. Comp.* **10**, 1038 (1989).
- <sup>45</sup>M. R. Roussel and S. J. Fraser, *J. Phys. Chem.* **97**, 8316 (1993).
- <sup>46</sup>W. P. Jones and S. Rigopoulos, *Combust. Theory Model.* **11**, 755 (2007).
- <sup>47</sup>R. J. Kee, J. F. Grcar, M. D. Smooke, and J. A. Miller, Sandia Report No. SAND85-8240, 1985.
- <sup>48</sup>R. L. G. M. Eggels and L. P. H. de Goeij, *Combust. Flame* **100**, 559 (1995).
- <sup>49</sup>O. Gicquel, D. Thévenin, M. Hilka, and N. Darabiha, *Combust. Theory Model.* **3**, 479 (1999).